

# Modeling enhanced firn densification due to strain softening

Falk M. Oraschewski<sup>1,2</sup> and Aslak Grinsted<sup>2</sup>

<sup>1</sup>Department of Geosciences, University of Tübingen, Tübingen, Germany.

<sup>2</sup>Physics of Ice, Climate, and Earth, Niels Bohr Institute, University of Copenhagen, Copenhagen, Denmark.

**Correspondence:** Falk M. Oraschewski (falk.oraschewski@uni-tuebingen.de)

**Abstract.** In the accumulation zone of glaciers and ice sheets snow is transformed into glacial ice by firn densification. Classically, this process is assumed to solely depend on temperature and overburden pressure which is controlled by the accumulation rate. However, exceptionally thin firn layers have been observed in the high-strain shear margins of ice streams. Previously, it has been proposed that this firn thinning can be explained by an enhancement of firn densification due to the effect of strain softening inherent to power-law creep. This hypothesis has not been validated, and the greater firn densities in the presence of horizontal strain rates have not yet been reproduced by models. Here, we develop a model that corrects the firn densification rate predicted by classical, climate-forced models for the effect of strain softening. With the model it is confirmed that strain softening dominates the firn densification process when high strain rates are present. Firn densities along a cross section of the North-East Greenland ice stream (NEGIS) are reproduced with good agreement, validating the accuracy of the developed model. Finally, it is shown that strain softening has significant implications for ice core dating and that it considerably affects the firn properties over wide areas of the polar ice sheet, even at low strain rates. Therefore, we suggest that, besides temperature and accumulation rate, horizontal strain rates should generally be considered as a forcing parameter in firn densification modeling.

## 1 Introduction

15 Firn densification refers to the transformation of snow into glacial ice, which occurs in the uppermost layers of ice sheets and glaciers within their accumulation zones, when old snow, now denoted as firn, is buried under younger snow. The overburden pressure gradually increases and causes densification of the firn. Large scale ice flow is not considered by firn models even though it is known that ice is a non-newtonian material where strain reduces the viscosity (Goldsby and Kohlstedt, 2001). In this paper, we demonstrate that this effect can have a substantial impact on firn densification.

20 Firn densification is conventionally divided into stages where different physical mechanisms dominate. Initially, the Newtonian grain-boundary sliding is dominant for densities of  $\rho \leq 550 \text{ kg m}^{-3}$ , which is referred to as stage 1 of firn densification (Alley, 1987). In stage 2, at densities of  $550 \text{ kg m}^{-3} \leq \rho \leq 830 \text{ kg m}^{-3}$ , the non-Newtonian dislocation creep, also known as power-law creep, dominates the densification process until bubble close-off (BCO) (Maeno and Ebinuma, 1983). Beyond this point, defined as the firn-ice transition, the further densification is slowed as the enclosed gas-bubbles get compressed and 25 eventually diffuse into the ice matrix (Salamatin et al., 1997).

For a variety of glaciological studies, properties of the firn need to be known. For example, it is essential to know the firn air content for deriving the mass balance of an ice sheet from changes of its surface elevation, measured by satellite altimetry (e.g. Helsen et al., 2008; Horlings et al., 2021). Ice core studies on the other hand require knowledge of the age difference  $\Delta\text{age}$  between the water and the gas records in the ice core. This age difference is primarily determined by the age of the firn at the 30 lock-in depth, where the air in the firn pores loses contact with the atmosphere (e.g. Schwander et al., 1997; Buijzer et al., 2015). The age at the lock-in depth is again closely related to the BCO age of the firn at the firn-ice transition.

In many applications, these properties are determined by employing a firn densification model. Over the years, a wide range of models have been developed (e.g. Herron and Langway, 1980; Alley, 1987; Arnaud et al., 2000; Arthern et al., 2010), which are adapted for different climatic conditions and application areas (Lundin et al., 2017). Stevens et al. (2020) provided with 35 the Community Firn Model (CFM) an open-source, modular model framework, which comprises the most established firn densification models within a one-dimensional Lagrangian modeling scheme and allows the implementation of additional firn processes as modular extensions.

While efforts are being made to directly model the physical processes that lead to densification of the firn (Alley, 1987; Arnaud et al., 2000; Arthern et al., 2010), empirically tuned models, such as the Herron-Langway model (HL, Herron and 40 Langway, 1980), are widely used. In this type of model, the densification rate equations are derived according to a few initial assumptions and subsequently tuned to fit density data from firn cores. Despite the different approaches, the majority of the existing models have in common that they merely consider temperature and accumulation rate as variable input parameters (Lundin et al., 2017). Only a few models take additional input parameters such as the impurity content into account (Bréant et al., 2017). Therefore, the classical models will be denoted as climate-forced in the following.

45 The limitation to climatic forcing is not only insufficient for finding firn model tuning parameters that are applicable for the whole Greenland ice sheet (Simonsen et al., 2013), but it also contradicts with observations of stress, or the corresponding strain, affecting the densification of firn (Zumberge et al., 1960; Crary and Wilson, 1961; Gow, 1968; Kirchner et al., 1979; Alley and Bentley, 1988; Riverman et al., 2019). As a consequence, existing firn models cannot sufficiently represent the reduced firn thickness that occurs in the high-strain shear margins of ice streams. However, the firn dynamics are important for 50 understanding the dynamics of ice streams, as they potentially control their stability and contribute to the formation of shear margins troughs (Christiansen et al., 2014; Riverman et al., 2019). The effect of horizontal strain rates on firn compaction moreover affects the firn air content in regions with strong ice dynamics and needs to be considered in mass balance studies (Horlings et al., 2021).

The reduced firn thickness due to strain is explained by two processes: Horizontal divergence and strain softening.  
55 Horizontal divergence of velocities causes a simple horizontal stretching and thus a vertical thinning of the firn. This effectively reduces the overburden load. The firn density itself is however not directly affected. Morris et al. (2017) accounted for this thinning in their firn model by introducing a correction factor that scales the vertical compaction strain rate according to the expected vertical thinning. A similar layer-thinning scheme was implemented into the CFM by Horlings et al. (2021) as an optional module.

60 Strain softening was first suggested by Alley and Bentley (1988) to accelerate the firn densification in the presence of horizontal strain rates. Alley and Bentley explain it by an enhancement of power-law creep, which as a non-Newtonian (pseudo-plastic) process scales with the square of the effective stress. Hence, a stress applied in horizontal direction can also accelerate the firn densification in vertical direction by reducing the effective viscosity. Strain softening mainly affects stage 2 of firn densification as this is where power-law creep is dominant (Alley and Bentley, 1988). This interpretation was supported by  
65 Riverman et al. (2019), who observed that the variation of firn thickness, recorded along a cross-section of the North-East Greenland Ice Stream (NEGIS) by active seismic surveying, correlates with the net strain along the flow path of the past 400 years.

70 Despite the observational evidence, firn densification models used for polar ice sheets do not capture the effect of strain softening. Based on a constitutive equation for the power-law creep of porous media (Duva and Crow, 1994), Gagliardini and Meyssonier (1997) have developed a glacier flow model that inherently considers compaction – and in particular strain softening – of the firn. It is widely used in studies of alpine glaciers (Lüthi and Funk, 2000; Zwinger et al., 2007; Licciulli et al., 2020), but has not been applied to the polar ice sheets. The reasons are presumably that this approach is computationally more expensive on large scales, more difficult to implement and that the range of conditions, that this model is calibrated and tested on, is not as wide as it is for the classical firn models.

75 In this paper, we aim to model the effect of strain softening in the firn with a different approach. We derive a scale factor that can be applied with any climate-forced firn densification model to correct its predicted firn densification rate for the impact of strain. Our approach is computationally cheap, simple to implement and thereby can extend the application range of the well-established classical firn models even further.

## 2 Theory

80 A firn densification model in a Lagrangian formulation expresses the densification rate of a firn layer as a function of external forcing parameters and internal parameters, representing its current state. The external parameters are generally time-variable. In a climate-forced model these are the temperature  $T$  and accumulation rate  $\dot{b}$  or the thereof derived overburden load  $\sigma$ . As an internal parameter most firn models only consider the current density  $\rho$  of the firn layer. Newly formed snow layers at the surface further require the initial snow density  $\rho_0$  as a boundary condition. For a specific site this parameter is in most  
85 applications however assumed to be constant with time. The densification rate of a climate-forced model (denoted with the subscript c) is hence given in the form of

$$\left( \frac{D\rho}{Dt} \right)_c = f(T, \sigma, \rho), \quad (1)$$

with the time  $t$ . Following Morris et al. (2017) this densification rate relates to a corresponding volumetric strain rate  $\dot{\varepsilon}_{\text{vol}}$ . In the classical one-dimensional case, where horizontal divergence is neglected, only densification in vertical direction is considered.  
90 In this case the volumetric strain rate matches the vertical component  $\dot{\varepsilon}_{zz,c}$ , which then reads as

$$\dot{\varepsilon}_{zz,c} = -\frac{1}{\rho} \left( \frac{D\rho}{Dt} \right)_c. \quad (2)$$

The densification rate given by a climate-forced model in this way directly translates into a vertical strain rate. Because in this case no additional horizontal strain rates are considered to affect firn densification, the strain rate tensor of such a model at a specific point in the firn is expressed by

$$95 \quad \dot{\varepsilon}_c = \begin{pmatrix} 0 & 0 & 0 \\ 0 & 0 & 0 \\ 0 & 0 & \dot{\varepsilon}_{zz,c} \end{pmatrix}. \quad (3)$$

However, horizontal flow will also strain the firn and the strain rate tensor more generally reads as

$$96 \quad \dot{\varepsilon} = \begin{pmatrix} \dot{\varepsilon}_{xx} & \dot{\varepsilon}_{xy} & \dot{\varepsilon}_{xz} \\ \dot{\varepsilon}_{xy} & \dot{\varepsilon}_{yy} & \dot{\varepsilon}_{yz} \\ \dot{\varepsilon}_{xz} & \dot{\varepsilon}_{yz} & \dot{\varepsilon}_{zz} \end{pmatrix}, \quad (4)$$

where the additional horizontal components ( $\dot{\varepsilon}_{xx}$ ,  $\dot{\varepsilon}_{xy}$ ,  $\dot{\varepsilon}_{yy}$ ) and vertical shear components ( $\dot{\varepsilon}_{xz}$ ,  $\dot{\varepsilon}_{yz}$ ) will affect the vertical strain rate  $\dot{\varepsilon}_{zz}$  by strain softening, such that  $\dot{\varepsilon}_{zz} \neq \dot{\varepsilon}_{zz,c}$ .

100 If the normal horizontal strain rate components do not balance ( $\dot{\varepsilon}_h = \dot{\varepsilon}_{xx} + \dot{\varepsilon}_{yy} \neq 0$ ), horizontal divergence is also active. Assuming that horizontal divergence only has a negligible influence on the pressure, which is justified for the second firn stage, where already a significant overburden pressure has built up, horizontal compression can be disregarded and the processes of strain softening and horizontal divergence can be taken as being independent of each other. Thus, the correction for horizontal divergence can be performed after the strain softening correction, following the layer thinning scheme by Morris et al. (2017) 105 and Horlings et al. (2021).

Thereby, the vertical strain rate effectively becomes  $\dot{\varepsilon}_{zz,tot} = \dot{\varepsilon}_{zz} - \dot{\varepsilon}_h$  and the volumetric strain rate is approximated by  $\dot{\varepsilon}_{zz}$  alone, because

$$106 \quad \dot{\varepsilon}_{vol} = \dot{\varepsilon}_{xx} + \dot{\varepsilon}_{yy} + \dot{\varepsilon}_{zz,tot} = \dot{\varepsilon}_{zz}. \quad (5)$$

Accordingly,  $\dot{\varepsilon}_{zz}$  translates back into the strain softening corrected densification rate

$$110 \quad \frac{D\rho}{Dt} = -\dot{\varepsilon}_{zz}\rho. \quad (6)$$

by taking Eq. 2 in reversed direction. From combining Eqs. 2 and 6 it then follows that

$$111 \quad \frac{D\rho}{Dt} = \frac{\dot{\varepsilon}_{zz}}{\dot{\varepsilon}_{zz,c}} \left( \frac{D\rho}{Dt} \right)_c. \quad (7)$$

Hence, the densification rate output of a climate-forced firn model can be corrected for the effect of strain softening by multiplication with a scale factor that is given by the ratio of the corresponding vertical strain rate components. We aim in the 115 following to determine this scale factor.

## 2.1 Constitutive relations for firn

Firn is a compressible material. Its deformation is generally given by two coupled constitutive relations which represent a rigid and a compressible phase. The former describes the relation between deviatoric stress and deviatoric strain rate, as given by

120 Glen's flow law for the deformation of incompressible ice (Glen, 1955; Nye, 1957). The relation of the compressible phase is set between the volumetric strain rate and the isotropic pressure.

125 While the proportionality factors between stress and strain, also denoted as effective viscosities, in the two constitutive relations generally differ, they are coupled in non-Newtonian materials by the fact that the strain rates of one phase also reduce the effective viscosity of the other. Duva and Crow (1994) formulated a constitutive relation for compressible power-law creeping materials and took account of the coupling by combining the relations of the two phases with corresponding weighting factors  $a$  and  $b$ . The ratio between these two factors essentially determines by how much the additional deviatoric strain rates reduce the effective viscosity of the compressible phase.

130 For firn the two weighting factors have been calibrated by Gagliardini and Meyssonier (1997) using firn density data of Site 2, Greenland. Unfortunately, the calibration is ill-posed and exactly the ratio of the weighting factors was fixed to solve the issue (Gagliardini, 2012). The factors  $a$  and  $b$  are therefore poorly constrained and in turn a scale factor based on the model by Gagliardini and Meyssonier (1997) would also be poorly constrained. To circumvent this issue, we will assume in the following that the effective viscosities of the two phases are equally affected by strain softening. This is feasible as we are not interested in the total effective viscosity of the compressible phase, but only in its relative change.

## 2.2 Compaction on the microscale

135 To motivate this approach and derive the scale factor, we look at firn compaction on a microscopic level, where firn is a mixture of solid ice and air. Internal stresses are concentrated at the contact areas between grains. Stress chains form which carry the overburden load (Peters et al., 2005). In the second firn stage, where grains have settled, the rate of compaction is controlled by how fast these chains deform.

The deformation of the solid ice matrix can be described by Glen's flow law (See also Fourteau et al., 2020),

$$\dot{\epsilon}_{\text{ice},ij} = A\tau_{\text{ice},E}^{n-1}\tau_{\text{ice},ij}, \quad (8)$$

140 with the deviatoric strain rate  $\dot{\epsilon}_{\text{ice}}$ , the deviatoric stress  $\tau_{\text{ice}}$  and the effective deviatoric stress  $\tau_{\text{ice},E}$ , which is the second invariant of the deviatoric stress tensor.  $A$  is the creep factor, which represents the temperature impact and  $n$  the creep exponent. As power-law creep is dominant in the second firn stage, we assume that other deformation processes can be disregarded.

Glen's flow law can equivalently be formulated in terms of the strain rate dependent effective viscosity  $\eta_{\text{ice}}$

$$\dot{\epsilon}_{\text{ice},ij} = \frac{1}{2\eta_{\text{ice}}}\tau_{\text{ice},ij} \\ \eta_{\text{ice}} = \left[2A^{1/n}\dot{\epsilon}_{\text{ice},E}^m\right]^{-1}, \quad (9)$$

145 with the exponent  $m = 1 - 1/n$ . The effective viscosity depends on the effective strain rate  $\dot{\epsilon}_{\text{ice},E}$ , which is a measure for the strength of deformation in the stress chains, given by the second invariant of the local deviatoric strain rate tensor.

In practice, it is difficult to apply Eq. 9 to densification as it would require detailed knowledge of the 3-dimensional structure of the ice-air matrix in order to relate how the overburden pressure is related to the deviatoric stress experienced throughout.

150 The overburden load tends to focus into stress chains such that the overburden is predominantly supported by relatively few ice grains (Peters et al., 2005). Most other grains will be shielded by these chains and will experience little deformation until it becomes their turn to carry the load.

155 To relate the microscopic deformation with the macroscopic firn compaction despite the difficulties, we need to make two simplifying assumptions: We expect that high macroscale deformation and compaction correlates with strong microscale deformation. Therefore, we assume that the microscale effective strain rate in the stress chains is proportional to the macroscopic effective strain rate  $\dot{\varepsilon}_E$  of the strain rate tensor that contains compaction (Eqs. 3 or 4), such that

$$\dot{\varepsilon}_{ice,E} = k_1 \cdot \dot{\varepsilon}_E, \quad (10)$$

where  $k_1$  is a scaling constant that we assume only depends on the material properties of the firn.

160 The second assumption is that the densification rate is controlled by the strain rate of the load-carrying grains as their deformation must be the limiting factor for the densification. Hence, we assume that the bulk behavior of the firn scales with the behavior of such characteristic grains, as follows:

$$\dot{\varepsilon}_{ij} = k_2 \cdot \dot{\varepsilon}_{ice,ij}, \quad (11)$$

where  $\dot{\varepsilon}_{ice,ij}$  represents a characteristic value of such grains, and  $k_2$  is again a material dependent scaling constant.

Applying the second assumption to Eq. 9 gives us

$$\dot{\varepsilon}_{zz} = \frac{k_2}{2\eta_{ice}} \tau_{ice,zz}, \quad (12)$$

165 where  $\tau_{ice,zz}$  is a characteristic deviatoric stress experienced by the grains that limit the deformation. We will assume that  $\tau_{ice,zz}$  only depends on load and the material properties of the firn, but is not affected by deformation in other directions.

### 2.3 The scale factor

170 Equations 8 to 12 are applicable independent of whether the additional strain rate components are considered. They can be formulated both in terms of the climate-forced model and the strain softening corrected model, with the only difference being whether the macroscopic effective strain rate is computed from Eq. 3 or 4. In particular,  $\kappa_1$ ,  $\kappa_2$  and  $\tau_{ice,zz}$  do not differ between the two cases as they are assumed to be independent of the additional strain rate components.

By dividing the two versions of Eq. 12, the firn strain rate ratio in Eq. 7, which is the scale factor, can be expressed in terms of a solid ice viscosity ratio:

$$\frac{\dot{\varepsilon}_{zz}}{\dot{\varepsilon}_{zz,c}} = \frac{\eta_{ice,c}}{\eta_{ice}}. \quad (13)$$

175 Inserting the expression for the ice viscosity (Eq. 9) and using Eq. 10 gives

$$\frac{\dot{\varepsilon}_{zz}}{\dot{\varepsilon}_{zz,c}} = \left( \frac{\dot{\varepsilon}_{ice,E}}{\dot{\varepsilon}_{ice,E,c}} \right)^m = \left( \frac{\dot{\varepsilon}_E}{\dot{\varepsilon}_{E,c}} \right)^m. \quad (14)$$

Thus, the enhancement from strain softening can be expressed in terms of macroscopic firn strain rates. By expanding the effective strain rates into components, we get

$$\frac{\dot{\varepsilon}_{zz}}{\dot{\varepsilon}_{zz,c}} = \left( \frac{\dot{\varepsilon}_{xx}^2 + \dot{\varepsilon}_{yy}^2 + \dot{\varepsilon}_{zz}^2 + 2\dot{\varepsilon}_{xy}^2 + 2\dot{\varepsilon}_{xz}^2 + 2\dot{\varepsilon}_{yz}^2}{\dot{\varepsilon}_{zz,c}^2} \right)^{m/2}, \quad (15)$$

180 which can be rewritten in the form of

$$r_v = (r_h^2 + r_v^2)^{m/2}, \quad (16)$$

whereby the following two variables are defined:

$$r_v := \frac{\dot{\varepsilon}_{zz}}{\dot{\varepsilon}_{zz,c}}, \quad (17)$$

$$r_h := \left( \frac{\dot{\varepsilon}_{xx}^2 + \dot{\varepsilon}_{yy}^2 + 2\dot{\varepsilon}_{xy}^2 + 2\dot{\varepsilon}_{xz}^2 + 2\dot{\varepsilon}_{yz}^2}{\dot{\varepsilon}_{zz,c}^2} \right)^{1/2}. \quad (18)$$

185 Existing purely climate driven densification models, such as the classical HL model, provide us with an estimate of the vertical strain rate ( $\dot{\varepsilon}_{zz,c}$ ) under the assumption that all other components of the strain rate tensor are zero (Eq. 2). The remaining components of  $r_h$  can be estimated from surface velocity observations or flow modeling. Their strength can be measured by the effective external strain rate  $\dot{\varepsilon}_{E,e} = [\frac{1}{2}(\dot{\varepsilon}_{xx}^2 + \dot{\varepsilon}_{yy}^2) + \dot{\varepsilon}_{xy}^2 + \dot{\varepsilon}_{xz}^2 + \dot{\varepsilon}_{yz}^2]^{1/2}$ .

In summary, all components of  $r_h$  are known and the variable  $r_v$  corresponds exactly to the scale factor that is sought. Hence, 190 Eq. 16 needs to be solved for  $r_v$  to obtain the scale factor for correcting the densification rate of a climate-forced model for the effect of strain softening.

The solution of Eq. 16 depends on the creep exponent. Dislocation creep is the key process driving densification in the second firn stage (Maeno and Ebinuma, 1983). In this paper we therefore use a creep exponent of  $n = 4$ , characteristic for dislocation creep (Goldsby and Kohlstedt, 2001; Bons et al., 2018). In this case, Eq. 16 is essentially a solvable polynomial of 195 order eight. Its solution is given by

$$\begin{aligned} \kappa_1 &= \left[ 9r_h^8 + \sqrt{81r_h^{16} + 768r_h^{18}} \right]^{1/3}, \\ \kappa_2 &= \left[ 1 + 8r_h^2 + \sqrt[3]{\frac{32}{9}\kappa_1} - \frac{\sqrt[3]{\frac{8192}{3}}r_h^6}{\kappa_1} \right]^{1/2}, \\ \kappa_3 &= \left[ \frac{1}{2} + 4r_h^2 - \frac{\kappa_1}{\sqrt[3]{18}} + \frac{\sqrt[3]{\frac{128}{3}}r_h^6}{\kappa_1} + \frac{1 + 12r_h^2 + 24r_h^4}{2\kappa_2} \right]^{1/2}, \\ r_v &= \left[ \frac{1}{4} + \frac{1}{4}\kappa_2 + \frac{1}{2}\kappa_3 \right]^{1/2}. \end{aligned} \quad (19)$$

An alternative solution for the often used case of  $n = 3$  is given in Oraschewski (2020).

The derivation of the strain softening enhancement above relies on a number of assumptions. We have assumed that in the second stage firn densifies by dislocation creep and that this densification is driven by vertical compression. Other densification 200 processes and horizontal compression are therefore assumed to be negligible and strain softening and horizontal divergence are assumed to be independent of each other. We have further assumed that the microscale solid ice deformation is the key process limiting the rate of firn densification. To relate this to the macroscale compaction we assume that the microscale effective strain rate of deformation scales with the macroscale effective strain rate that contains compaction (Eq. 10) and that firn strain rates 205 scale with a characteristic value for the solid ice strain rate (Eq. 11). The scaling constants ( $k_1$  and  $k_2$ ) and the characteristic vertical deviatoric stress of the rate-limiting grains ( $\tau_{\text{ice},zz}$ ) are assumed to have no directional dependence but can depend on density, microstructure, temperature, and load. From these assumptions follows that the effective viscosities in the constitutive equations of the rigid and the compressible phase in the firn are assumed to be equally affected when additional strain rates soften the firn. In this way, we could obtain a model for the enhancement of firn densification by strain softening that involves zero free parameters.

## 210 2.4 Regularization

The densification in climate-forced models, such as the HL model, is characterized by an exponential decay towards the density of solid ice. The vertical strain rate  $\dot{\varepsilon}_{zz,c}$  in such models goes to zero as the firn density approaches the density of ice of  $917 \text{ kg m}^{-3}$ . Thereby,  $r_h$  and with it the scale factor  $r_v$  go towards infinity. This singularity causes a nonphysical behavior of the strain softening model, where the density of ice is approached almost instantaneously at a certain point.

215 To circumvent this issue, a regularization is introduced. Inspired by *regularized Glen's flow law* (Greve and Blatter, 2009, Ch. 4) a residual strain rate  $\dot{\varepsilon}_0$  is added to the vertical strain rate to ensure a finite correction factor:

$$r_h := \left( \frac{\dot{\varepsilon}_{xx}^2 + \dot{\varepsilon}_{yy}^2 + \dot{\varepsilon}_{zz}^2 + 2\dot{\varepsilon}_{xy}^2 + 2\dot{\varepsilon}_{xz}^2 + 2\dot{\varepsilon}_{yz}^2}{(\dot{\varepsilon}_{zz,c} + \dot{\varepsilon}_0)^2} \right)^{1/2}. \quad (20)$$

Leaving the perspective of firn densification modeling, the residual strain rate can be associated with the general thinning of firn and ice layers in ice sheets that is induced by the flow of ice towards the ice sheet margins. While the densification 220 part of the vertical strain rate approaches zero, this contribution remains finite. The residual strain rate can be obtained by flow modeling or measured using strain gauge instruments (Zumberge et al., 2002; Elsberg et al., 2004) or phase-sensitive radar (Gillet-Chaulet et al., 2011; Zeising and Humbert, 2021).

## 2.5 Tuning bias correction

Empirical climate-forced firn models contain two tuning parameters which represent the dependency and sensitivity of the 225 densification rate to temperature and accumulation rate. They are obtained by tuning the model to firn density measurements from, for example, firn cores, whereby it is assumed that all inter-site density variability can be attributed to the variability of temperature and accumulation rate between the sites. If another process that is driven by a different forcing parameter also affects the densification, its contribution will be implicitly captured by the two tuning parameters for the climatic forcing.

Thereby, the additional process is not only inadequately represented, but also the model sensitivity to the climatic forcing will

230 be inaccurate. We refer to the implicit contribution as a tuning bias.

In Sect. 5 we show evidence that neglecting strain softening can cause such a tuning bias. If the firn cores that were used to tune the model were subjected to a mean effective external strain rate of  $\bar{\varepsilon}_{E,e}$ , it can be expected that the model outputs approximately capture a strain softening enhancement that corresponds to a strain rate forcing of that size. As a consequence, this contribution would be considered twice when our strain softening enhancement is applied to a tuning biased empirical firn

235 model.

The densification rate output of the climate-forced model therefore actually has to be seen as the densification rate by climatic forcing alone  $(D\rho/Dt)_0$  times the scaling factor  $r_{cor}$  for strain softening due to an effective strain rate of  $\dot{\varepsilon}_{cor} = \bar{\varepsilon}_{E,e}$ :

$$\left( \frac{D\rho}{Dt} \right)_c = r_{cor} \left( \frac{D\rho}{Dt} \right)_0. \quad (21)$$

As given in Eq. 7 our scale factor is applied to the biased densification rate of the climate forced model  $(D\rho/Dt)_c$ , whereas 240 it is assumed that the input densification rate is unbiased. To correct for the tuning bias, the strain softening scale factor has to be divided by  $r_{cor}$ , whereby Eq. 7 is replaced by

$$\frac{D\rho}{Dt} = \frac{r_v}{r_{cor}} \left( \frac{D\rho}{Dt} \right)_c. \quad (22)$$

With this equation the strain softening model has no effect when the effective strain rate input  $\dot{\varepsilon}_{E,e}$  matches  $\dot{\varepsilon}_{cor}$ . In the case of  $\dot{\varepsilon}_{E,e} < \dot{\varepsilon}_{cor}$  the densification rate will be slowed.

245 Correctly determining  $r_{cor}$  is actually prevented by the fact that the unbiased densification rate  $(D\rho/Dt)_0$  is unknown. As a first-order approximation we therefore compute it based on the output of the climate forced model, analogously to the computation of the scale factor  $r_v$ . Deriving the tuning bias correction from the biased model output itself will induce a small error into the also relatively small correction. In the overall picture, it will be a tiny error that can be neglected.

### 3 Application of the model

250 Our new model for strain softening (Eq. 19) takes the form of a scale factor to classical, climate-forced models. It allows us to calculate how much faster firn densifies when the firn pack is exposed to e.g. horizontal strain rates. The quality of the fit to the overall density profile at a single site is therefore a product of both the quality of the chosen classical density model and the quality of the applied scale factor. The scale factor is widely applicable to many different firn densification models. In this paper, we want to isolate and focus on the impact of the scale factor rather than the combined effect. Equation 7 models 255 the change in densification rate. Thus, the validation of the model must also focus on whether it is able to reproduce density changes between different strain environments. We will therefore test the predictions of the strain enhancement model on data collected at NEGIS, where large variations in horizontal strain rates, and thus in  $r_h$ , occur within a relatively small area.

### 3.1 Assumption of depth uniformity

For the application of the model, we assume in this paper that the horizontal velocities in the firn are uniform with depth.

260 While, from a theoretical point of view, this assumption is not needed in the strain softening model, it is required due to the lack of internal velocity data. This has two consequences: First, horizontal strain rates ( $\dot{\varepsilon}_{xx}$ ,  $\dot{\varepsilon}_{yy}$ , and  $\dot{\varepsilon}_{xy}$ ) are also assumed to be independent of depth in the firn column. And second, the vertical shear rates ( $\dot{\varepsilon}_{xz}$  and  $\dot{\varepsilon}_{yz}$ ) are assumed to be negligible in comparison to the horizontal strain rates. These assumptions allow to estimate the numerator of  $r_h$  (Eq. 18) from surface velocities alone.

265 When the strain softening enhancement is applied to the interior of the Greenland (GrIS) and Antarctic ice sheets (AIS), as we do here, this is justified. In ice sheets vertical shear is predominantly confined to the deepest layers (e.g. Gundestrup et al., 1993; Weikusat et al., 2017), whereas firn only accounts for a small, upper fraction of the total ice thickness over the majority of the ice sheet. The change of horizontal velocities in the firn will therefore be negligible. This is also a common first approximation in ice core dating, as for example the Dansgaard and Johnsen (1969) model assumes that horizontal velocities 270 are near uniform with depth in the upper half of the ice sheet.

Although the uppermost firn layers are softer and therefore more likely to entail vertical shear (See Schwerzmann, 2006, Fig. 5.2), this can also be neglected in the interior of the ice sheets. Due to their flat surface, a driving force is missing that can induce such shear. But even if vertical shear would occur in the top layers, this could safely be ignored in our model, because the very soft layers are located in firn stage 1, whereas strain softening first becomes important in firn stage 2.

275 As the main application area of the model are the polar ice sheets and not alpine glaciers, where the Gagliardini and Meyssonnier (1997) model is more suitable, the model is currently implemented such that only depth uniform horizontal strain rates are considered, but nonetheless, it is principally possible to take nonuniform and vertical shear rates into account when they are known for the study site by e.g. bore hole deformation.

According to the assumption that the horizontal strain rates solely determine the strength of the strain softening, their 280 magnitude will in the following be expressed by the effective horizontal strain rate  $\dot{\varepsilon}_{E,h} = [\frac{1}{2}(\dot{\varepsilon}_{xx}^2 + \dot{\varepsilon}_{yy}^2) + \dot{\varepsilon}_{xy}^2]^{1/2}$ , which replaces the effective external strain rate that was used before.

### 3.2 Implementation

The strain softening scale model is implemented as an optional module into the CFM by Stevens et al. (2020). Supported by its Lagrangian modeling scheme, the implementation itself is rather simple and computationally cheap. The uncorrected 285 vertical strain rate is computed from the initial densification rate according to Eq. 2 using a classical densification model. In combination with the strain rate input data, the variable  $r_h$  can then be computed by Eq. 20, from which the correction factor of the vertical strain rate is computed with Eq. 19 and applied according to Eq. 7 or 22, depending on whether the tuning bias correction is applied.

In order to reduce the number of input parameters for the horizontal strain rate from three ( $\dot{\varepsilon}_{xx}$ ,  $\dot{\varepsilon}_{xy}$ ,  $\dot{\varepsilon}_{yy}$ ) to two, they are  
290 loaded in the form of the principal horizontal strain rates (see e.g. Nye, 1959). In this way, the shear components disappear,  
such that the amount of input data is reduced without the loss of any relevant information.

The strain softening model is only applied in the second stage of firn densification for  $\rho > 550 \text{ kg m}^{-3}$  as power-law creep is  
thought to dominate firn densification only in this range, while the Newtonian grain-boundary sliding is driving the densification  
295 process before. Although a smooth transition between the two processes over a range of densities is expected (Hörhold et al.,  
2011), its exact form is unknown and a sharp transition is assumed in our present implementation. Nonetheless, attempts to  
implement a smooth transition did not affect the model output significantly (not shown).

Within the CFM framework the strain softening model can be executed in combination with any of the implemented climate-  
forced firn densification models. In the following model experiments, we will use the Herron-Langway model (Herron and  
300 Langway, 1980) in its stress-based formulation as the input model. While the HL model on one hand is capable of reproducing  
the firn densities in the investigated NEGIS region accurately, its stress-based formulation additionally considers potential  
strain-induced changes of the overburden load, which an accumulation-based formulation would not capture. Temperature  
evolution will not be modeled in our experiments, as our focus lies on processes happening in the second firn stage, where  
seasonal temperature variations are damped by heat conduction.

## 4 Data

305 Modeling strain softening requires knowledge about the horizontal strain rates. For the modeling experiments conducted in  
this paper, horizontal strain rates are computed from surface velocity maps of the GrIS and AIS using the logarithmic strain  
rate computation method as discussed by Alley et al. (2018). Nominal computation of the strain rates proved however to be  
sufficient as differences between the two computation methods were smaller than the uncertainty induced by the velocity data  
itself.

310 For the GrIS horizontal strain rates are computed from the MEaSUREs Multi-year Greenland Ice Sheet Velocity Mosaic  
(Joughin et al., 2016, 2018), which has a spatial resolution of  $250 \text{ m} \times 250 \text{ m}$ . The ice sheet margins are set following the  
MEaSUREs Greenland Ice Mapping Project (GIMP) Land Ice and Ocean Classification Mask (Howat, 2017; Howat et al.,  
2014). For the AIS the MEaSUREs InSAR-Based Antarctica Ice Velocity Map, Version 2 (Rignot et al., 2017, 2011; Mouginot  
et al., 2012) with a spatial resolution of  $450 \text{ m} \times 450 \text{ m}$  is used.

315 Before determining the strain rates from the velocity fields, a Gaussian filter is applied on the velocity maps to reduce the  
impact of processing artifacts in the data, which likely were caused by combining velocity data from different sources for  
producing these velocity fields. These artifacts appear as a grid structure in the strain rate products and clearly do not represent  
any physical information, but would lead to an overestimation of the horizontal strain rates, if not removed. For the GrIS  
velocity data, a Gaussian filter with a standard deviation of 2 pixels is applied. For the AIS we use a variable Gaussian filter  
320 with standard deviations between 2 – 10 pixels. Regions with poor data coverage and higher reported uncertainties — e.g. in  
the polar hole — are smoothed more. The smoothing reduces the effective spatial resolution of the velocity grid, which can

dampen local strain maxima for example in ice stream shear margins. However, this is not a major concern, because km-scale variations of horizontal strain rates average out over the firn age.

Using the strain rate products, the mean of the effective horizontal strain rates at the locations of the firn cores that were used to tune the HL model is determined, whereby Little America V site is excluded, as no data exist for this point. We obtain a value of  $\dot{\varepsilon}_{\text{cor}} = 4.5 \times 10^{-4} \text{ yr}^{-1}$ , which we use for the tuning bias correction in the following.

For validating the strain softening model, firn density data recorded at the NEGIS in the vicinity of the EGRIP ice core site are used. As suggested by Vallelonga et al. (2014) the NEGIS with its high-strain shear margins offers excellent opportunities for studying firn densification processes. The data reproduced in this study comprise a 37 km-long cross section of the NEGIS firn densities recorded with active seismic surveying by Riverman et al. (2019) and the density of the NEGIS firn core (Vallelonga et al., 2014). Their locations are shown in Fig. 1. Additionally, the density of the EGRIP S5 2019 shear margin firn core is modeled with the intent to compare the model with directly measured firn density data from a high-strain area. However, this data are unfortunately not available yet, as the firn core is stored at the EGRIP station and is not accessible, because of COVID-19-related restrictions of field work.

The horizontal strain rates that the firn at these sites has experienced in the past are computed by step-wise backtracing their position according to the velocity field with a monthly resolution and interpolating the computed horizontal strain rate components to these points at every time step.

We force the model with a constant temperature of  $-29.9^\circ\text{C}$ . This is the seasonality-corrected mean of the 10 m temperature recorded between June 2019 and January 2021 at the PROMICE weather station at EGRIP (Fausto and van As, 2019; Fausto et al., 2021). Using a constant temperature input is justified because we are mainly interested in firn processes occurring below a depth of 10 m, where seasonal and inter-annual variability of temperature is smoothed out by heat conduction. Further, we do not expect a significant spatial variability of temperature over this relatively small study region.

As accumulation rate input we use the values derived by Riverman et al. (2019) from the Accumulation Radar of an Operation IceBridge flightline (Paden et al., 2014, updated 2018) crossing the NEGIS density profile, see Fig. 1b. We extrapolate the accumulation rate from the flight line to the sites where densification is modeled using nearest point interpolation. At NEGIS the surface density is set to  $295 \text{ kg m}^{-3}$ , which is the density measured in the top 10 cm in this region by Schaller et al. (2016). For the residual strain rate a value of  $\dot{\varepsilon}_0 = -0.7 \times 10^{-4} \text{ yr}^{-1}$  is applied, following observation at EGRIP by Zeising and Humbert (2021).

The effect of strain softening on firn densification is not only studied on local, but also on ice sheet wide scales. For this purpose, the output data of the regional climate model HIRHAM5, forced by the ERA-Interim reanalysis product (Dee et al., 2011), are employed as climatic forcing. For the GrIS the mean of the precipitation and surface temperature output between 1980 and 2014 with a spatial resolution of  $0.05^\circ$  or  $\sim 5 \text{ km}$  are used (Langen et al., 2017; Mottram et al., 2017). For the AIS the mean surface mass balance and 10 m temperature output between 1980 and 2017 are used (Hansen et al., 2021), which have a resolution of  $0.11^\circ$  or  $\sim 12.5 \text{ km}$ .

New surface layers are formed with a density of  $315 \text{ kg m}^{-3}$ , following Fausto et al. (2018). Although there will be a high variability of the surface density over the whole GrIS and AIS, the potential bias can be neglected in our studies, as the main

interest lies in the identification of the relative changes of the firn properties by strain softening, rather than in absolute values. The residual strain rate in the ice sheet experiments is set to  $-2 \times 10^{-4} \text{ yr}^{-1}$ , which is a good approximation of the vertical strain rate when compared to ice sheet and ice rise observations (Zumberge et al., 2002; Elsberg et al., 2004; Gillet-Chaulet et al., 2011).

## 5 Results and Discussion

### 5.1 Sensitivity test

In order to understand how strain softening behaves under different dynamic conditions a sensitivity test is conducted. For the climatic conditions present at the EGRIP site, the firn density and age are modeled for a range of effective horizontal strain rates between  $\dot{\varepsilon}_{E,H} = 0$  and  $\dot{\varepsilon}_{E,H} = 7 \times 10^{-3} \text{ yr}^{-1}$ .

The strain dependent age profile of the firn is shown in Fig. 2a. The black contour lines additionally indicate the transition between first and second firn stage at the critical density of  $550 \text{ kg m}^{-3}$  and the firn-ice transition at the BCO density of  $830 \text{ kg m}^{-3}$ . The depth of the critical density remains unaffected, as the strain enhancement model is only active in the second firn stage. Below the critical density the densification is accelerated as the effective horizontal strain rate is increased and the firn-ice transition occurs at shallower depths. This reduction is strongest at low  $\dot{\varepsilon}_{E,H}$  and steadily gets weaker when strain rates rise. For example the thinning at an effective strain rate of about  $1.2 \times 10^{-3} \text{ yr}^{-1}$  is already half as big as in the case of  $\dot{\varepsilon}_{E,H} = 7 \times 10^{-3} \text{ yr}^{-1}$ . Hence, the sensitivity of firn densification to strain softening is greatest at low strain rates.

The picture is similar for the sensitivity of the firn age at a certain depth and the BCO age, represented in Fig. 2a by the age of the firn at the BCO density line. Again both quantities are most sensitive to the effect of strain softening at low strain rates. The shift of the firn age at a given depth is however rather weak with a decrease of the firn age by up to 10 % for  $\dot{\varepsilon}_{E,H} = 7 \times 10^{-3} \text{ yr}^{-1}$ . The BCO age in contrast is strongly affected by the horizontal strain rates with a decrease of 50 % at the highest strain rate values in the test.

In summary, both the BCO depth as well as the BCO age are strongly affected by high strain rates, but even low strain rates of less than  $1 \times 10^{-3} \text{ yr}^{-1}$  do affect the firn properties considerably. Especially this fact highlights the need for the tuning bias correction. Due to the initially strong effect of strain softening, an implicit contribution of  $\dot{\varepsilon}_{\text{cor}} = 4.5 \times 10^{-4} \text{ yr}^{-1}$ , as it was observed for the HL model, already matters.

### 5.2 Comparison with firn cores

The firn density profiles at the sites of the NEGIS and the EGRIP S5 2019 firn cores are modeled with the HL model by first considering no strain and subsequently activating the modules for horizontal divergence (not shown), strain softening and the tuning bias correction (TBC).

In Fig. 2b the results for the NEGIS firn core, drilled at the site of the EGRIP station, are shown and compared to the data. The mean effective horizontal strain rate over the firn age at this site is indicated by the corresponding vertical line in 2a at

390  $\overline{\dot{\varepsilon}_{E,h}} = 0.42 \times 10^{-3} \text{ yr}^{-1}$ . As it is small, the differences between the various model setups are also small. The no-strain model already reproduces the density data with good agreement. Horizontal divergence only contributes to a reduction of the firn thickness by 1 m and strain softening thins the firn by additional 7 m.

As the no-strain model already matches the data, the strain softening enhancement leads to an underestimation of the firn thickness. But by this fact, the tuning bias becomes apparent and the underestimation should not be attributed to the strain softening model, but to the underlying HL model.  $\overline{\dot{\varepsilon}_{E,h}}$  almost matches  $\dot{\varepsilon}_{cor}$ . Accordingly, the firn cores used for tuning the HL model have on average experienced as much stain as the firn at EGRIP and the corresponding strain softening contribution can 395 be expected to be already captured by the HL model. As a consequence, this contribution is considered twice, when our strain softening enhancement model is applied. In order to only consider it once, the previously introduced tuning bias correction has to be added. It increases the firn thickness again by around 7 m and thereby suppresses the effect of the strain softening model.

400 Although the shear margin firn density data of the S5 2019 firn core are not available, the corresponding modeled firn density profiles are shown in Fig. 2c as an example for a high-strain site with  $\overline{\dot{\varepsilon}_{E,h}} = 2.9 \times 10^{-3} \text{ yr}^{-1}$ . The modeled density profile for the cases of no strain resembles the profiles at the EGRIP site. Horizontal divergence again only has a minor effect on the firn profile and is not shown. Strain softening causes a significant reduction of the firn thickness by 30 m and thereby causes the kink at the critical density to disappear. Yet, the tuning bias in the HL model is expected to be as big as on the EGRIP site and the correction for it increases the firn thickness again by 7 m.

405 As before, these numbers have to be understood in the way that at the S5 site strain softening causes firn thinning of 30 m, but 7 m thereof are already captured by the HL model, giving a total reduction 23 m when the strain softening enhancement and tuning bias correction are applied.

### 5.3 Validation with NEGIS firn density cross section

410 As a next step, the firn densities recorded by Riverman et al. (2019) along a cross section of NEGIS are reproduced. The original data are shown in Fig. 3a with the firn-ice transition being indicated by the white contour line. In this profile the increased firn density within the shear margins of NEGIS can be seen, causing a reduction of the firn thickness by 20 to 30 m.

In Fig. 3b the density profile is modeled with the tuning bias corrected strain softening model at the locations of the individual seismic survey sites as shown in Fig. 1a, according to the forcing parameters displayed in Fig. 3c, which are the accumulation rate  $\dot{b}$  and the mean effective horizontal strain rate over the firn age  $\overline{\dot{\varepsilon}_{E,H}}$ . For the temperature, a constant value of  $-29.9^\circ\text{C}$  was assumed. The solid white line indicates the BCO depth of the corrected strain softening model. Additionally, it is also 415 displayed for the model runs with no strain, horizontal divergence and the uncorrected strain softening model.

In the case of no strain, the BCO line represents the impact of the accumulation rate variability alone. It shows that the observed density peaks in the shear margins cannot be attributed to the accumulation pattern. In contradistinction to the observed lower firn thickness, the higher snow accumulation in the shear margin would even promote an increase of the firn thickness.

420 Similar conclusions need to be drawn for the effect of horizontal divergence, as the corresponding BCO line only differs slightly from the case of no strain. Horizontal divergence merely affects the firn thickness by a few meters, whereat no clear trend for a firn thinning can be seen, but instead, firn thickness also increases where velocities are actually converging as it is

for example the case at the S5 2019 firn core site, indicated by the left vertical line. If on a flat ice sheet velocities diverge at one place, they tend to converge elsewhere. Therefore, horizontal divergence cannot explain a pure firn thinning pattern but always results in an increase of firn thickness nearby. Consequently, horizontal divergence cannot explain the reduced firn thickness in  
425 the shear margins of ice streams.

The increased shear margin firn density with the respective lowering of the BCO depth can only be reproduced, when strain softening is included in the model. In this case the extent of the density peaks can be reproduced well, which validates the model and supports the idea that the enhanced firn densification rates in high-strain environments are caused by strain softening.

Comparing the strain softening cases, modeled with and without applying the tuning bias correction, it becomes notable,  
430 that even the small contribution of  $\dot{\varepsilon}_{\text{cor}}$  can considerably alter the modeled firn thickness by around 7 m. The impact of the correction only varies little over the cross section as the climatic forcing also varies little. Therefore, the correction basically reduces the initial densification rate of the HL model equally over the whole section before the strain softening enhancement is applied.

Outside the ice stream, where effective horizontal strain rate forcing is even lower than  $\dot{\varepsilon}_{\text{cor}}$ , the firn thickness is increased.  
435 Thereby, the fit of the tuning bias corrected strain softening model is not only better in the high-strain shear margins, but also in the low-strain sections of the profile. This indicates that the tuning bias correction and the sensitivity of the model are accurate. It especially supports our interpretation that some fixed implicit strain softening contribution is captured in the Herron-Langway model – and potentially also in other empirical climate-forced firn models – and that this contribution will lead to a mismatch of the model, whenever the site-specific strain rate forcing differs from the forcing that caused the tuning  
440 bias.

The main difference between data and model in Fig. 3b lies in an apparent shift of the modeled firn density profile of 2 km towards south-east. No processing error that would explain such a shift could be identified, neither in the model nor in the data. Instead, the shift could point towards a potential movement of the ice stream position over time, which would not be represented in the model, because the past horizontal strain rates are inferred from present-day surface velocities, whereby the  
445 assumption of steady state conditions is implicitly made.

## 5.4 Firn properties along NEGIS

In Fig. 4a the modeled change of the firn thickness is compared with the elevation of the ice sheet surface along the seismic survey line. The shear margin troughs resemble the modeled reduction of the firn thickness with regard to depth, extent and location, suggesting that they are formed by a collapse of the firn layer due to strain softening. However, as the agreement is  
450 not perfect, other factors, such as upstream effects, accumulation variations and the sub-glacial topography, must also alter the surface elevation and the structure of the shear margins troughs.

Previously, the expected depth of these troughs was estimated by integrating the vertical strain rate caused by horizontal divergence along the flow line, giving a total strain of  $-0.1$  which translates into a trough depth of 200 to 300 m (Fahnestock et al., 2001). Our results on the contrary indicate that horizontal divergence in the firn does not contribute to the trough  
455 formation. Although our study focuses on the firn layer, this conclusion can be extended to the ice layer below. Because the

460 firn thinning matches the depression of the surface topography, the ice layer itself has an approximately flat surface, suggesting that no thinning is occurring within it. Instead, it indicates that the pattern of horizontal strain rates must be changing with depth. This in turn might have an impact on strain softening, which is not captured in the presented model, as we assume that horizontal strain rates are constant with depth. Hence, the internal dynamics at the ice stream shear margins and the impact of the depth-variable strain rates need to be investigated in future studies.

465 The BCO age along the profile is shown in Fig. 4b. While the firn reaches an age of up to 400 yr in the center of the ice stream, the firn-ice transition in the shear margin already takes place after about 200 yr. This means that in the shear margins the densification rate is effectively doubled by strain softening. The BCO age is reduced by 50 % over a distance of only 5 km, whereas the climatic forcing on firn air processes can be expected to vary little over such short distances. For this reason, we suggest to exploit the shear margins as a natural laboratory for firn air studies, in order to better constrain characteristic parameters of firn air processes.

## 5.5 Implications for ice core dating

470 The gas enclosed in bubbles at the lock-in depth is younger than the surrounding ice. This introduces a difference between the age of the ice matrix and the gas in an ice core ( $\Delta$ age). Accurate models of densification are thus important for synchronizing ice core records. Precise relative timing is necessary to understand the sequence of events and the physical mechanisms behind past changes in climate (Pedro et al., 2012). For example Buizert et al. (2015) find that abrupt Greenland warming events lead corresponding Antarctic cooling onsets by  $218 \pm 92$  yr. This conclusion hinges on the estimated  $\Delta$ age at the WAIS Divide ice core. In contrast, Svensson et al. (2020) find a  $122 \pm 24$  yr lag between Greenland and Antarctic ice core records using a volcanic synchronization that does not rely on densification processes.

475 To gauge the potential impact of strain softening at this site, we test the sensitivity of the firn age to an exemplary effective strain rate of  $1 \times 10^{-3}$  yr $^{-1}$  using WAIS Divide climate conditions. Therefore, the strain softening model without the tuning bias correction is applied in order to obtain the total contribution by strain softening. For Holocene climate we find that an effective strain rate of  $1 \times 10^{-3}$  yr $^{-1}$  reduces the BCO age, which we use as an approximation of  $\Delta$ age, by 23 % (from 309 to 238 yr) and BCO depth by 20 %. For Last Glacial Maximum conditions ( $-41^\circ\text{C}$  and  $0.1$  m yr $^{-1}$ ) the BCO age is reduced by 480 33 % or 209 yr and BCO depth by 29 %.

485 Accordingly, strain softening can affect the  $\Delta$ age in two ways: On the one hand, it is reduced when strain rates rise. Accordingly, if the flow pattern has changed in the past, strain rates might have been different. At sites where this is the case, tuning a firn densification model to the local Holocene conditions can still induce a bias in the  $\Delta$ age estimates inferred for the past. On the other hand, the impact of strain softening depends on the climatic forcing at the site itself and can alter over time even if the effective horizontal strain rate remains constant. In our sensitivity test for the WAIS Divide site, the BCO age reduction by a moderate strain rate forcing decreased from 209 to 71 yr between the Last Glacial Maximum and the Holocene.

The decrease of the age difference by strain softening, as well as its variability under stable dynamic conditions, is therefore on the order of the observed time lag between Greenland and Antarctic ice core records and needs to be considered for synchronizing them by the methane (CH<sub>4</sub>) record. The shift of  $\Delta$ age can thereby be positive or negative. A climate forced model

490 which has been calibrated to the locally observed density profile will implicitly account for the local present-day horizontal strain rate. Depending on whether past horizontal strain rates were greater or smaller than at present, the strain softening correction to such a model can also work in either direction. We stress that our WAIS Divide modeling only constitutes a sensitivity test and should not be taken as an error estimate of existing firn models which are tightly constrained by the present-day firn density profile and  $\delta^{15}\text{N}$  data (Buizert et al., 2015).

495 In classical climate-forced densification models the densification rate and thus  $\Delta\text{age}$  is almost entirely determined by surface temperature and accumulation rate. Buizert et al. (2021) exploit this to infer past surface temperature from estimates of  $\Delta\text{age}$  and accumulation rate. However, our modeling shows that horizontal strain leads to enhanced densification rates and should also be taken into account. The large-scale ice flow could have changed over time, which complicates the modeling of past densification rates. Indeed, accumulation changes must be accompanied by changes in ice flow speeds, and thus strain rates, 500 in order to maintain flux balance. While the results by Buizert et al. (2021) agree with the temperature inferred from borehole thermometry, our observations highlight that in regions with a strong dynamical history strain softening needs to be considered. The opposition of these observations can however also be used to infer an upper limit for the past strain rates, if the firn densification-derived temperatures are backed up by an independent method.

## 5.6 Firn properties of the polar ice sheets

505 Finally, the ice sheet wide impact of strain softening on firn densification is studied. For this purpose, a range of steady-state firn density profiles are modeled with the HL model and the strain softening extension, but without the tuning bias correction being applied, to create a data grid that can be used to obtain the approximate change of the BCO depth and BCO age by strain softening at every point on the ice sheet in a computationally efficient manner by interpolation. These profiles encompass various combinations of forcing parameters that cover the range of climatic conditions and effective horizontal strain rates that 510 are present over the GrIS and the AIS according to the multi-year average of the HIRHAM5 output data and the satellite-based velocity field products.

For Greenland, temperature was altered between  $-29^\circ\text{C}$  and  $-17^\circ\text{C}$  in steps of  $2^\circ\text{C}$ , accumulation rate was logarithmically increased in 7 steps from  $75 \text{ mm yr}^{-1}$  to  $1 \text{ m yr}^{-1}$  and the effective horizontal strain rate was increased in steps of  $1 \times 10^{-3} \text{ yr}^{-1}$  from 0 to  $7 \times 10^{-3} \text{ yr}^{-1}$ , giving 392 different combinations of forcing parameters in total. For Antarctica temperature was 515 linearly increased from  $-60^\circ\text{C}$  to  $-10^\circ\text{C}$  in 6 steps, accumulation rate was again logarithmically increased in 9 steps from  $5 \text{ mm yr}^{-1}$  to  $1 \text{ m yr}^{-1}$  and the effective horizontal strain rate was increased up to  $10 \times 10^{-3} \text{ yr}^{-1}$  with the same spacing as before. Which gives 594 different combinations for the AIS.

Locations with warmer temperatures and lower accumulation rates than given by these input ranges were not modeled and for the GrIS also places with an average annual melt of more than 1 mm were excluded. This was done because in the ablation zone 520 of the polar ice sheets additional processes like melt-water percolation and refreezing contribute to firn densification, which will not be enhanced by strain softening. Drawing conclusions about how strain softening affects the general firn densification process in these areas is therefore not easily possible. To not overestimate the contribution of strain softening in these areas, we decided to restrict our studies to the dry zone of the polar ice sheets by introducing the above restrictions.

525 The BCO depth and BCO age for the input forcing were then determined from the modeled steady-state firn profiles. Local firn properties at every point on the ice sheet were obtained by linear interpolation of the local climatic forcing to the parameter grid. With this approach the ice sheet wide contribution of strain softening to firn densification can be studied by comparing the interpolated firn thickness in the cases of no strain to the case when the uncorrected strain softening model is employed.

530 Figure 5 shows for both polar ice sheets the firn thickness when strain softening is considered (a & d), as well as the absolute (b & e) and the relative (c & f) change of the firn thickness that is caused by strain softening. The figure illustrates that strain softening on both ice sheets significantly reduces the firn thickness in the shear margins of ice streams and the onset regions of the outlet glaciers. A considerable contribution is also observed over the fast-flowing Antarctic ice shelves. When looking at the relative firn thinning of the AIS in Fig. 5f, it can moreover be noted that even in the interior of the East Antarctic ice sheet (EAIS) strain softening enhances firn densification by up to 10 %, despite low flow velocities and therefore also low horizontal strain rates being present. This unexpected observation can be explained by very low temperatures and accumulation rates 535 occurring in this region, which give rise to extremely low firn densification rates with a BCO age on the order of  $10^3$  yr and in consequence enable strain softening to have a relatively strong impact by being active over a long period.

540 However, strain rates derived from remotely sensed velocities are sensitive to the degree of smoothing applied. Spatially uncorrelated velocity noise will lead to a positive bias in the effective strain rate. Smoothing reduces the noise amplitude and will act to lessen this bias. Unfortunately, smoothing will also blur the true strain rate signal leading to a negative bias in the effective strain rate in high-strain regions. The degree of smoothing is therefore a compromise between reducing noise, and not degrading the signal too much. In this paper, we have chosen the degree of smoothing necessary to remove obvious 545 artifacts. However, in the interior regions with very slow flow the true strain rates may be so small that even a tiny remaining noise amplitude can still be a substantial component of the estimated effective strain rate. This is an important caveat when interpreting the continental scale maps in Fig. 5. For example the observed strain softening contribution in the interior of the EAIS could therefore also be caused by an overestimation of the strain rates due to remaining noise.

The velocity maps moreover contain spots in the polar hole, where data are missing and where it therefore is not possible to model the effect of strain softening. In combination with the difficulties arising from processing artifacts and noise, this highlights the need for high-quality velocity and strain rate data from remote sensing for modeling the effect of strain softening.

550 Nonetheless, we see that the strain softening contribution to firn densification matters over wide areas of the ice sheets. This however does not mean that existing firn densification models, which do not consider strain softening, generally overestimate the firn thicknesses, but rather that these models will likely include some contribution of strain softening in the form of a tuning bias, as previously discussed. To highlight this effect, Fig. 5 additionally shows the locations of the firn cores that were 555 used for empirically tuning the Herron-Langway model. At least at some of these sites, especially on the AIS, firn thickness is appreciably affected by strain softening, which supports our interpretation that the HL model will capture this thinning to some extent.

As we have seen in Fig. 2b, the HL model without any adaptations fits well at the EGRIP site, but it does for the wrong reason because only by chance the strain rate forcing at this site matches the implicit forcing in the HL model. At sites where the effective horizontal strain rate is different, the fit of the HL model is lower. Consequently, strain softening is potentially

the reason why often site-specific recalibration of firn models is needed and why the firn properties over the whole GrIS  
560 cannot sufficiently be modeled by only considering climatic forcing, as observed by Simonsen et al. (2013). Imagining that the magnitude of the tuning bias differs between various firn models, strain softening can in turn also contribute to the mismatch between different firn models, as seen by (Lundin et al., 2017).

To take account of this implicit contribution, we introduced the tuning bias correction, which is however only a first-order estimate of the implicit strain softening contribution. We want to stress that it is required to consider all three input parameters  
565 – i.e. the accumulation rate, the temperature and the effective horizontal strain rate – during the empirical tuning of a firn model to represent all of them accurately and to capture the sensitivity of firn densification to the three forcing parameters correctly. We leave this to future studies.

## 6 Conclusions

We have developed an extension for firn densification models that is capable of correcting the densification rate of any climate-  
570 forced firn model for the effect of strain softening. Employing this model, it was studied how strain softening affects firn densification on local and ice sheet wide scales.

We found that the sensitivity of firn densification to strain softening is highest at low strain rates and that therefore even low strain rates can affect the firn thickness considerably in areas where forcing by accumulation rate and temperature is weak. In high-strain areas, such as the shear margins of ice streams, a significant acceleration of firn densification by strain softening was  
575 modeled, which is in good agreement with observations of lower firn thickness in these areas. As other potential processes, like horizontal divergence or a greater accumulation in the shear margin troughs, could not explain this reduction of firn thickness, our work supports the idea that strain softening is the principal cause. It was further observed that the change of firn thickness resembles the lowering of the surface elevation in the shear margins, which suggests that the shear margin troughs form because of a faster settling of the firn due to strain softening.

580 Strain softening does not only affect the firn thickness but also reduces the age of the firn at the firn-ice transition. According to our model this can lead to a reduction of the BCO age by around 50 % over a few kilometers in the shear margin of ice streams. We therefore suggest to exploit this feature as a natural laboratory in future firn air studies, because the climatic forcing over such small distances will only vary slightly. Moreover, strain softening can strongly alter the BCO age over time, even at constant, moderate strain rates. For ice core dating this induces a bias in the BCO age, which previously has not been  
585 taken into account, but is on a considerable order for synchronizing ice core records by CH<sub>4</sub>.

Finally, we demonstrate that strain softening has a substantial effect on firn densification over wide areas of ice sheets, and as a consequence that horizontal strain rates should generally be considered in firn densification modeling, because a restriction to climatic forcing parameters results in a misrepresentation of the latter. Our work therefore suggests that besides temperature and accumulation rate also the effective horizontal strain rate should be considered as a relevant forcing parameter  
590 in firn densification modeling and that all three parameters should already be considered during the empirical tuning of firn densification models.

*Code availability.* The code for the CFM model with the extension for strain softening is available at <https://github.com/oraschewski/CommunityFirnModel/tree/Falk>.

*Author contributions.* The idea for the strain softening model extension was developed by both authors. F. Oraschewski carried out the model 595 experiments and wrote the majority of the code and paper, based on his Master's thesis. A. Grinsted acted as a supervisor for the thesis as well as in the preparation of the manuscript.

*Competing interests.* The authors declare that they have no conflict of interest.

*Acknowledgements.* We acknowledge the support of the Villum Investigator Project IceFlow (grant no. 16572) for this work and the support 600 of the German Academic Scholarship Foundation to F. Oraschewski. EGRIP is directed and organized by the Centre for Ice and Climate at the Niels Bohr Institute, University of Copenhagen. It is supported by funding agencies and institutions in Denmark (A. P. Møller Foundation, University of Copenhagen), USA (US National Science Foundation, Office of Polar Programs), Germany (Alfred Wegener Institute, Helmholtz Centre for Polar and Marine Research), Japan (National Institute of Polar Research and Arctic Challenge for Sustainability), Norway (University of Bergen and Trond Mohn Foundation), Switzerland (Swiss National Science Foundation), France (French Polar Institute Paul-Emile Victor, Institute for Geosciences and Environmental research), Canada (University of Manitoba) and China (Chinese Academy 605 of Sciences and Beijing Normal University). We further acknowledge the Arctic and Climate Research section at the Danish Meteorological Institute for producing and making available their HIRHAM5 model output. Data from the Programme for Monitoring of the Greenland Ice Sheet (PROMICE) were provided by the Geological Survey of Denmark and Greenland (GEUS) at <http://www.promice.dk>. We also acknowledge the use of the the National Snow and Ice Data Center QGreenland package, the Quantarctica package provided by the Norwegian Polar Institute and the use of data provided by the SCAR Antarctic Digital Database. We thank Kiya Riverman for providing the firn density 610 and accumulation rate data across NEGIS and Helle Astrid Kjær and Paul Vallelonga for providing the NEGIS firn core data. We thank Nicholas Rathmann for discussions on porous flow.

## References

Alley, K. E., Scambos, T. A., Anderson, R. S., Rajaram, H., Pope, A., and Haran, T. M.: Continent-wide estimates of Antarctic strain rates from Landsat 8-derived velocity grids, *J. Glaciol.*, 64, 321–332, <https://doi.org/10.1017/jog.2018.23>, 2018.

615 Alley, R. B.: Firn densification by grain-boundary sliding: A first model, *J. Phys. Colloq.*, 48, C1–249–C1–256, <https://doi.org/10.1051/jphyscol:1987135>, 1987.

Alley, R. B. and Bentley, C. R.: Ice-core analysis on the Siple Coast of West Antarctica, *Ann. Glaciol.*, 11, 1–7, <https://doi.org/10.3189/S0260305500006236>, 1988.

620 Arnaud, L., Barnola, J. M., and Duval, P.: Physical modeling of the densification of snow/firn and ice in the upper part of polar ice sheets, in: Physics of ice core records, pp. 285–305, Hokkaido University Press, <http://hdl.handle.net/2115/32472>, 2000.

Arthern, R. J., Vaughan, D. G., Rankin, A. M., Mulvaney, R., and Thomas, E. R.: In situ measurements of Antarctic snow compaction compared with predictions of models, *J. Geophys. Res.*, 115, F03011, <https://doi.org/10.1029/2009JF001306>, 2010.

Bons, P. D., Kleiner, T., Llorens, M.-G., Prior, D. J., Sachau, T., Weikusat, I., and Jansen, D.: Greenland ice sheet: Higher nonlinearity of ice flow significantly reduces estimated basal motion, *Geophys. Res. Lett.*, 45, 6542–6548, <https://doi.org/10.1029/2018GL078356>, 2018.

625 Bréant, C., Martinerie, P., Orsi, A., Arnaud, L., and Landais, A.: Modelling firn thickness evolution during the last deglaciation: constraints on sensitivity to temperature and impurities, *Clim. Past*, 13, 833–853, <https://doi.org/10.5194/cp-13-833-2017>, 2017.

Buizert, C., Cuffey, K. M., Severinghaus, J. P., Bagenstos, D., Fudge, T. J., Steig, E. J., Markle, B. R., Winstrup, M., Rhodes, R. H., Brook, E. J., Sowers, T. A., Clow, G. D., Cheng, H., Edwards, R. L., Sigl, M., McConnell, J. R., and Taylor, K. C.: The WAIS Divide deep ice core WD2014 chronology – Part 1: Methane synchronization (68–31 ka BP) and the gas age–ice age difference, *Clim. Past*, 11, 153–173, <https://doi.org/10.5194/cp-11-153-2015>, 2015.

630 Buizert, C., Fudge, T. J., Roberts, W. H. G., Steig, E. J., Sherriff-Tadano, S., Ritz, C., Lefebvre, E., Edwards, J., Kawamura, K., Oyabu, I., Motoyama, H., Kahle, E. C., Jones, T. R., Abe-Ouchi, A., Obase, T., Martin, C., Corr, H., Severinghaus, J. P., Beaudette, R., Epifanio, J. A., Brook, E. J., Martin, K., Chappellaz, J., Aoki, S., Nakazawa, T., Sowers, T. A., Alley, R. B., Ahn, J., Sigl, M., Severi, M., Dunbar, N. W., Svensson, A., Fegyveresi, J. M., He, C., Liu, Z., Zhu, J., Otto-Btiesner, B. L., Lipenkov, V. Y., Kageyama, M., and Schwander, J.: Antarctic surface temperature and elevation during the Last Glacial Maximum, *Science*, 372, 1097–1101, <https://doi.org/10.1126/science.abd2897>, 2021.

635 Christianson, K., Peters, L. E., Alley, R. B., Anandakrishnan, S., Jacobel, R. W., Riverman, K. L., Muto, A., and Keisling, B. A.: Dilatant till facilitates ice-stream flow in northeast Greenland, *Earth Planet. Sc. Lett.*, 401, 57–69, <https://doi.org/10.1016/j.epsl.2014.05.060>, 2014.

Crary, A. P. and Wilson, C. R.: Formation of “blue” glacier ice by horizontal compressive forces, *J. Glaciol.*, 3, 1045–1050, <https://doi.org/10.3189/S0022143000017445>, 1961.

640 Dansgaard, W. and Johnsen, S. J.: A flow model and a time scale for the ice core from Camp Century, Greenland, *J. Glaciol.*, 8, 215–223, <https://doi.org/10.3189/S0022143000031208>, 1969.

Dee, D. P., Uppala, S. M., Simmons, A. J., Berrisford, P., Poli, P., Kobayashi, S., Andrae, U., Balmaseda, M. A., Balsamo, G., Bauer, P., Bechtold, P., Beljaars, A. C. M., van de Berg, L., Bidlot, J., Bormann, N., Delsol, C., Dragani, R., Fuentes, M., Geer, A. J., Haimberger, L., Healy, S. B., Hersbach, H., Hólm, E. V., Isaksen, L., Kållberg, P., Köhler, M., Matricardi, M., McNally, A. P., Monge-Sanz, B. M., Morcrette, J.-J., Park, B.-K., Peubey, C., de Rosnay, P., Tavolato, C., Thépaut, J.-N., and Vitart, F.: The ERA-Interim reanalysis: configuration and performance of the data assimilation system, *Q. J. Roy. Meteor. Soc.*, 137, 553–597, <https://doi.org/10.1002/qj.828>, 2011.

Duva, J. M. and Crow, P. D.: Analysis of consolidation of reinforced materials by power-law creep, *Mech. Mater.*, 17, 25–32, [https://doi.org/10.1016/0167-6636\(94\)90011-6](https://doi.org/10.1016/0167-6636(94)90011-6), 1994.

650 Elsberg, D. H., Harrison, W. D., Zumberge, M. A., Morack, J. L., Pettit, E. C., Waddington, E. D., and Husmann, E.: Depth- and time-dependent vertical strain rates at Siple Dome, Antarctica, *J. Glaciol.*, 50, 511–521, <https://doi.org/10.3189/172756504781829684>, 2004.

Fahnestock, M. A., Joughin, I., Scambos, T. A., Kwok, R., Krabill, W. B., and Gogineni, S.: Ice-stream-related patterns of ice flow in the interior of northeast Greenland, *J. Geophys. Res.-Atmos.*, 106, 34 035–34 045, <https://doi.org/10.1029/2001JD900194>, 2001.

655 Fausto, R. S. and van As, D.: Programme for Monitoring of the Greenland Ice Sheet (PROMICE): Automatic weather station data. Version: v03, Geological Survey of Denmark and Greenland (GEUS) [data set], <https://doi.org/10.22008/promice/data/aws>, 2019.

Fausto, R. S., Box, J. E., Vandecrux, B., van As, D., Steffen, K., MacFerrin, M. J., Machguth, H., Colgan, W., Koenig, L. S., McGrath, D., Charalampidis, C., and Braithwaite, R. J.: A snow density dataset for improving surface boundary conditions in Greenland ice sheet firn modeling, *Front. Earth Sci.*, 6, 51, <https://doi.org/10.3389/feart.2018.00051>, 2018.

660 Fausto, R. S., van As, D., Mankoff, K. D., Vandecrux, B., Citterio, M., Ahlstrøm, A. P., Andersen, S. B., Colgan, W., Karlsson, N. B., Kjeldsen, K. K., Korsgaard, N. J., Larsen, S. H., Nielsen, S., Pedersen, A. Ø., Shields, C. L., Solgaard, A. M., and Box, J. E.: Programme for Monitoring of the Greenland Ice Sheet (PROMICE) automatic weather station data, *Earth Syst. Sci. Data*, 13, 3819–3845, <https://doi.org/10.5194/essd-13-3819-2021>, 2021.

Fourteau, K., Gillet-Chaulet, F., Martinerie, P., and Faïn, X.: A micro-mechanical model for the transformation of dry polar firn into ice using the level-set method, *Front. Earth Sci.*, 8, 101, <https://doi.org/10.3389/feart.2020.00101>, 2020.

665 Gagliardini, O.: Porous Law for snow and firn in Elmer/Ice, <http://elmerfem.org/elmerice/wiki/lib/exe/fetch.php?media=solvers:poroussolver.pdf>, 2012.

Gagliardini, O. and Meyssonier, J.: Flow simulation of a firn-covered cold glacier, *Ann. Glaciol.*, 24, 242–248, <https://doi.org/10.3189/S0260305500012246>, 1997.

670 Gillet-Chaulet, F., Hindmarsh, R. C. A., Corr, H. F. J., King, E. C., and Jenkins, A.: *In-situ* quantification of ice rheology and direct measurement of the Raymond Effect at Summit, Greenland using a phase-sensitive radar, *Geophys. Res. Lett.*, 38, L24503, <https://doi.org/10.1029/2011GL049843>, 2011.

Glen, J. W.: The creep of polycrystalline ice, *P. Roy Soc. Lond. A Mat.*, 228, 519–538, <https://doi.org/10.1098/rspa.1955.0066>, 1955.

Goldsby, D. L. and Kohlstedt, D. L.: Superplastic deformation of ice: Experimental observations, *J. Geophys. Res.-Sol.*, 106, 11 017–11 030, <https://doi.org/10.1029/2000JB900336>, 2001.

675 Gow, A. J.: Deep core studies of the accumulation and densification of snow at Byrd Station and Little America V, Antarctica, CRREL Research Report, 197, 1–45, <http://hdl.handle.net/11681/5803>, 1968.

Greve, R. and Blatter, H.: *Dynamics of Ice Sheets and Glaciers*, Springer, Berlin, Heidelberg, first edn., <https://doi.org/10.1007/978-3-642-03415-2>, 2009.

Gundestrup, N. S., Dahl-Jensen, D., Hansen, B. L., and Kelty, J.: Bore-hole survey at Camp Century, 1989, *Cold Reg. Sci. Technol.*, 21, 187–193, [https://doi.org/10.1016/0165-232X\(93\)90006-T](https://doi.org/10.1016/0165-232X(93)90006-T), 1993.

680 Hansen, N., Langen, P. L., Boberg, F., Forsberg, R., Simonsen, S. B., Thejll, P., Vandecrux, B., and Mottram, R.: Downscaled surface mass balance in Antarctica: impacts of subsurface processes and large-scale atmospheric circulation, *The Cryosphere*, 15, 4315–4333, <https://doi.org/10.5194/tc-15-4315-2021>, 2021.

685 Helsen, M. M., van den Broeke, M. R., van de Wal, R. S. W., van de Berg, W. J., van Meijgaard, E., Davis, C. H., Li, Y., and Goodwin, I.: Elevation changes in antarctica mainly determined by accumulation variability, *Science*, 320, 1626–1629, <https://doi.org/10.1126/science.1153894>, 2008.

690 Herron, M. M. and Langway, C. C.: Firn densification: an empirical model, *J. Glaciol.*, 25, 373–385, <https://doi.org/10.1017/S0022143000015239>, 1980.

Hörhold, M. W., Kipfstuhl, S., Wilhelms, F., Freitag, J., and Frenzel, A.: The densification of layered polar firn, *J. Geophys. Res.-Earth*, 116, F01 001, <https://doi.org/10.1029/2009JF001630>, 2011.

695 Horlings, A. N., Christianson, K., Holschuh, N., Stevens, C. M., and Waddington, E. D.: Effect of horizontal divergence on estimates of firn-air content, *J. Glaciol.*, 67, 287–296, <https://doi.org/10.1017/jog.2020.105>, 2021.

Howat, I.: MEaSUREs Greenland Ice Mapping Project (GIMP) Land Ice and Ocean Classification Mask, Version 1., Boulder, Colorado USA. NASA National Snow and Ice Data Center Distributed Active Archive Center [data set], <https://doi.org/10.5067/B8X58MQBFUPA>, 2017.

695 Howat, I. M., Negrete, A., and Smith, B. E.: The Greenland Ice Mapping Project (GIMP) land classification and surface elevation data sets, *The Cryosphere*, 8, 1509–1518, <https://doi.org/10.5194/tc-8-1509-2014>, 2014.

Joughin, I., Smith, B. E., Howat, I. M., and Scambos, T. A.: MEaSUREs Multi-year Greenland Ice Sheet Velocity Mosaic, Version 1., Boulder, Colorado USA. NASA National Snow and Ice Data Center Distributed Active Archive Center [data set], <https://doi.org/10.5067/QUA5Q9SVMSJG>, 2016.

700 Joughin, I., Smith, B. E., and Howat, I. M.: A complete map of Greenland ice velocity derived from satellite data collected over 20 years, *J. Glaciol.*, 64, 1–11, <https://doi.org/10.1017/jog.2017.73>, 2018.

Kirchner, J. F., Bentley, C. R., and Robertson, J. D.: Lateral density differences from seismic measurements at a site on the Ross Ice Shelf, Antarctica, *J. Glaciol.*, 24, 309–312, <https://doi.org/10.3189/S0022143000014829>, 1979.

705 Langen, P. L., Fausto, R. S., Vandecrux, B., Mottram, R. H., and Box, J. E.: Liquid water flow and retention on the Greenland ice sheet in the regional climate model HIRHAM5: Local and large-scale impacts, *Front. Earth Sci.*, 4, 110, <https://doi.org/10.3389/feart.2016.00110>, 2017.

Licciulli, C., Bohleber, P., Lier, J., Gagliardini, O., Hoelzle, M., and Eisen, O.: A full Stokes ice-flow model to assist the interpretation of millennial-scale ice cores at the high-Alpine drilling site Colle Gnifetti, Swiss/Italian Alps, *J. Glaciol.*, 66, 35–48, <https://doi.org/10.1017/jog.2019.82>, 2020.

710 Lundin, J. M. D., Stevens, C. M., Arthern, R., Buijzer, C., Orsi, A., Ligtenberg, S. R. M., Simonsen, S. B., Cummings, E., Essery, R., Leahy, W., Harris, P., Helsen, M. M., and Waddington, E. D.: Firn Model Intercomparison Experiment (FirnMICE), *J. Glaciol.*, 63, 401–422, <https://doi.org/10.1017/jog.2016.114>, 2017.

Lüthi, M. and Funk, M.: Dating ice cores from a high Alpine glacier with a flow model for cold firn, *Ann. Glaciol.*, 31, 69–79, <https://doi.org/10.3189/172756400781820381>, 2000.

715 Maeno, N. and Ebinuma, T.: Pressure sintering of ice and its implication to the densification of snow at polar glaciers and ice sheets, *J. Phys. Chem.*, 87, 4103–4110, <https://doi.org/10.1021/j100244a023>, 1983.

Morris, E. M., Mulvaney, R., Arthern, R. J., Davies, D., Gurney, R. J., Lambert, P., De Rydt, J., Smith, A. M., Tuckwell, R. J., and Winstrup, M.: Snow densification and recent accumulation along the iSTAR traverse, Pine Island Glacier, Antarctica, *J. Geophys. Res.-Earth*, 122, 2284–2301, <https://doi.org/10.1002/2017JF004357>, 2017.

720 Mottram, R., Boberg, F., Langen, P., Yang, S., Rodehacke, C., Christensen, J. H., and Madsen, M. S.: Surface mass balance of the Greenland ice sheet in the regional climate model HIRHAM5: Present state and future prospects, *Low Temperature Science*, 75, 105–115, <https://doi.org/10.14943/lowtemsci.75.105>, 2017.

Mouginot, J., Scheuchl, B., and Rignot, E.: Mapping of ice motion in Antarctica using synthetic-aperture radar data, *Remote Sens.*, 4, 2753–2767, <https://doi.org/10.3390/rs4092753>, 2012.

725 Nye, J. F.: The distribution of stress and velocity in glaciers and ice-sheets, *P. Roy Soc. Lond. A Mat.*, 239, 113–133, <https://doi.org/10.1098/rspa.1957.0026>, 1957.

Nye, J. F.: A method of determining the strain-rate tensor at the surface of a glacier, *J. Glaciol.*, 3, 409–419, <https://doi.org/10.1017/S0022143000017093>, 1959.

730 Oraschewski, F.: Modelling of firn densification in the presence of horizontal strain rates, M.Sc. Thesis, University of Copenhagen, Copenhagen, Denmark, <https://doi.org/10.31237/osf.io/fdhxg>, 2020.

Paden, J., Li, J., Leuschen, C., Rodriguez-Morales, F., and Hale, R.: IceBridge Accumulation Radar L1B Geolocated Radar Echo Strength Profiles, Version 2, Boulder, Colorado: NASA National Snow and Ice Data Center DAAC [data set], <https://doi.org/10.5067/0ZY1XYHNIQNY>, 2014, updated 2018.

Pedro, J. B., Rasmussen, S. O., and van Ommen, T. D.: Tightened constraints on the time-lag between Antarctic temperature and CO<sub>2</sub> during 735 the last deglaciation, *Clim. Past*, 8, 1213–1221, <https://doi.org/10.5194/cp-8-1213-2012>, 2012.

Peters, J. F., Muthuswamy, M., Wibowo, J., and Tordesillas, A.: Characterization of force chains in granular material, *Phys. Rev. E*, 72, 041307–1–041307–8, <https://doi.org/10.1103/PhysRevE.72.041307>, 2005.

Rignot, E., Mouginot, J., and Scheuchl, B.: Ice flow of the Antarctic ice sheet, *Science*, 333, 1427–1430, <https://doi.org/10.1126/science.1208336>, 2011.

740 Rignot, E., Mouginot, J., and Scheuchl, B.: MEaSUREs InSAR-Based Antarctica Ice Velocity Map, Version 2, Boulder, Colorado USA. NASA National Snow and Ice Data Center Distributed Active Archive Center [data set], <https://doi.org/10.5067/D7GK8F5J8M8R>, 2017.

Riverman, K. L., Alley, R. B., Anandakrishnan, S., Christianson, K., Holschuh, N. D., Medley, B., Muto, A., and Peters, L. E.: Enhanced firn densification in High-Accumulation shear margins of the NE greenland ice stream, *J. Geophys. Res.-Earth*, 124, 365–382, <https://doi.org/10.1029/2017JF004604>, 2019.

745 Salamatin, A. N., Lipenkov, V. Y., and Duval, P.: Bubbly-ice densification in ice sheets: I. Theory, *J. Glaciol.*, 43, 387–396, <https://doi.org/10.3189/S0022143000034961>, 1997.

Schaller, C. F., Freitag, J., Kipfstuhl, S., Laepple, T., Steen-Larsen, H. C., and Eisen, O.: A representative density profile of the North Greenland snowpack, *The Cryosphere*, 10, 1991–2002, <https://doi.org/10.5194/tc-10-1991-2016>, 2016.

Schwander, J., Sowers, T., Barnola, J.-M., Blunier, T., Fuchs, A., and Malaizé, B.: Age scale of the air in the summit ice: Implication for 750 glacial-interglacial temperature change, *J. Geophys. Res.-Atmos.*, 102, 19 483–19 493, <https://doi.org/10.1029/97JD01309>, 1997.

Schwerzmann, A. A.: Borehole analysis and flow modeling of firn-covered cold glaciers, Ph.D. thesis, ETH Zurich, Zurich, Switzerland, <https://doi.org/10.3929/ETHZ-A-005114924>, 2006.

755 Simonsen, S. B., Stenseng, L., Aðalgeirsdóttir, G., Fausto, R. S., Hvidberg, C. S., and Lucas-Picher, P.: Assessing a multilayered dynamic firn-compaction model for Greenland with ASIRAS radar measurements, *J. Glaciol.*, 59, 545–558, <https://doi.org/10.3189/2013JoG12J158>, 2013.

Stevens, C. M., Verjans, V., Lundin, J. M. D., Kahle, E. C., Horlings, A. N., Horlings, B. I., and Waddington, E. D.: The Community Firn Model (CFM) v1.0, *Geosci. Model Dev.*, 13, 4355–4377, <https://doi.org/10.5194/gmd-13-4355-2020>, 2020.

Svensson, A., Dahl-Jensen, D., Steffensen, J. P., Blunier, T., Rasmussen, S. O., Vinther, B. M., Vallelonga, P., Capron, E., Gkinis, V., Cook, E.,  
760 Kjær, H. A., Muscheler, R., Kipfstuhl, S., Wilhelms, F., Stocker, T. F., Fischer, H., Adolphi, F., Erhardt, T., Sigl, M., Landais, A., Parrenin,  
F., Buizert, C., McConnell, J. R., Severi, M., Mulvaney, R., and Bigler, M.: Bipolar volcanic synchronization of abrupt climate change  
in Greenland and Antarctic ice cores during the last glacial period, *Clim. Past*, 16, 1565–1580, <https://doi.org/10.5194/cp-16-1565-2020>,  
2020.

765 Vallelonga, P., Christianson, K., Alley, R. B., Anandakrishnan, S., Christian, J. E. M., Dahl-Jensen, D., Gkinis, V., Holme, C., Jacobel, R. W.,  
Karlsson, N. B., Keisling, B. A., Kipfstuhl, S., Kjær, H. A., Kristensen, M. E. L., Muto, A., Peters, L. E., Popp, T., Riverman, K. L.,  
Svensson, A. M., Tibuleac, C., Vinther, B. M., Weng, Y., and Winstrup, M.: Initial results from geophysical surveys and shallow coring of  
the Northeast Greenland Ice Stream (NEGIS), *The Cryosphere*, 8, 1275–1287, <https://doi.org/10.5194/tc-8-1275-2014>, 2014.

Weikusat, I., Jansen, D., Binder, T., Eichler, J., Faria, S. H., Wilhelms, F., Kipfstuhl, S., Sheldon, S., Miller, H., Dahl-Jensen, D., and Kleiner,  
770 T.: Physical analysis of an Antarctic ice core—towards an integration of micro- and macrodynamics of polar ice, *Philos. T. Roy. Soc. A.*,  
375, 20150347, <https://doi.org/10.1098/rsta.2015.0347>, 2017.

Zeising, O. and Humbert, A.: Indication of high basal melting at the EastGRIP drill site on the Northeast Greenland Ice Stream, *The  
Cryosphere*, 15, 3119–3128, <https://doi.org/10.5194/tc-15-3119-2021>, 2021.

Zumberge, J. H., Giovinetto, M., Kehle, R., and Reid, J.: Deformation of the Ross Ice Shelf near the Bay of Whales, Antarctica, IGY  
775 Glaciological Report Series (New York, IGY World Data Center A, Glaciology, American Geographical Society), 3, 1960.

Zumberge, M. A., Elsberg, D. H., Harrison, W. D., Husmann, E., Morack, J. L., Pettit, E. C., and Waddington, E. D.:  
Measurement of vertical strain and velocity at Siple Dome, Antarctica, with optical sensors, *J. Glaciol.*, 48, 217–225,  
<https://doi.org/10.3189/172756502781831421>, 2002.

Zwinger, T., Greve, R., Gagliardini, O., Shiraiwa, T., and Lylly, M.: A full Stokes-flow thermo-mechanical model for firn and ice applied to  
780 the Gorshkov crater glacier, Kamchatka, *Ann. Glaciol.*, 45, 29–37, <https://doi.org/10.3189/172756407782282543>, 2007.

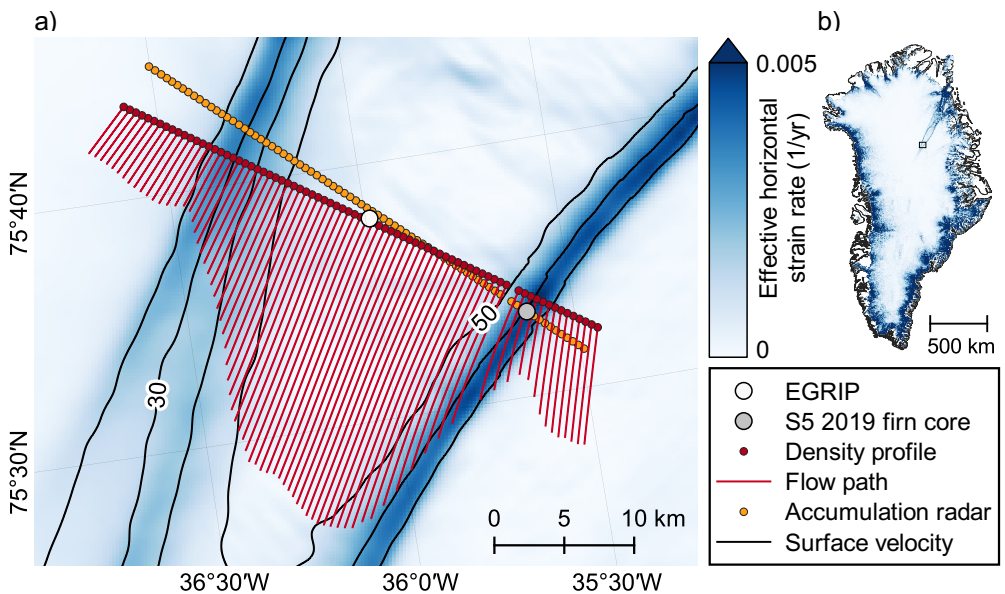


**Figure 1.** (a) Locations of firn surveys conducted at NEGIS around the EGRIP station. The map shows the sites of the NEGIS firn core (at EGRIP) and the S5 2019 firn core. The red dots indicate the coordinates of the active seismic surveying sites that form the density profile by Riverman et al. (2019) and the yellow dots the corresponding closest points on the Operation IceBridge accumulation radar line. The red lines indicate the backtraced flow path over the firn age at the density profile points. In the background, the effective horizontal strain rate and surface velocity contours (in  $\text{m yr}^{-1}$ ) are shown. (b) Effective horizontal strain rate over the Greenland ice sheet. The black box outlines the extent of (a).

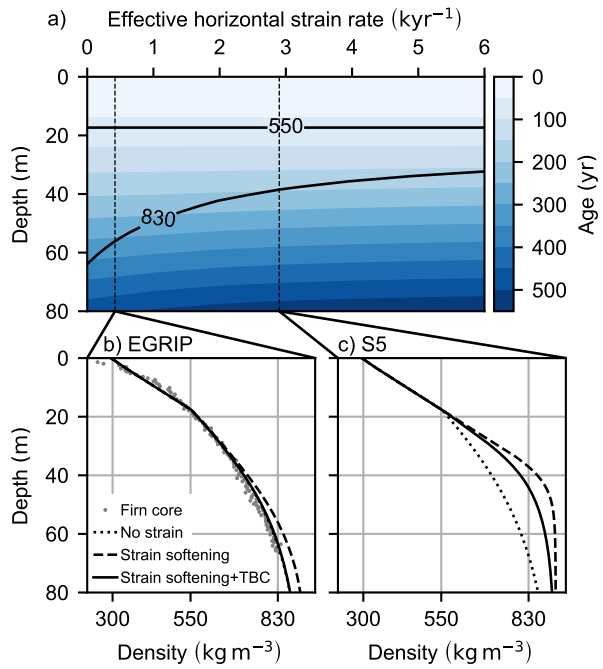


**Figure 2.** (a) Study of the decreasing sensitivity of firn densification to strain softening for increasing effective horizontal strain rates for climatic conditions present at EGRIP. The background shows the age contours and the black lines indicate the critical depth and the depth of the firn-ice transition. Vertical dashed lines indicate the backtraced mean effective horizontal strain rate at the firn core sites in (b) and (c). (b) Firn density data and models of the NEGIS firn core at EGRIP and its model with no strain, strain softening and additionally the tuning bias correction (TBC) being applied. (c) The same model outputs for the S5 2019 shear margin firn core.

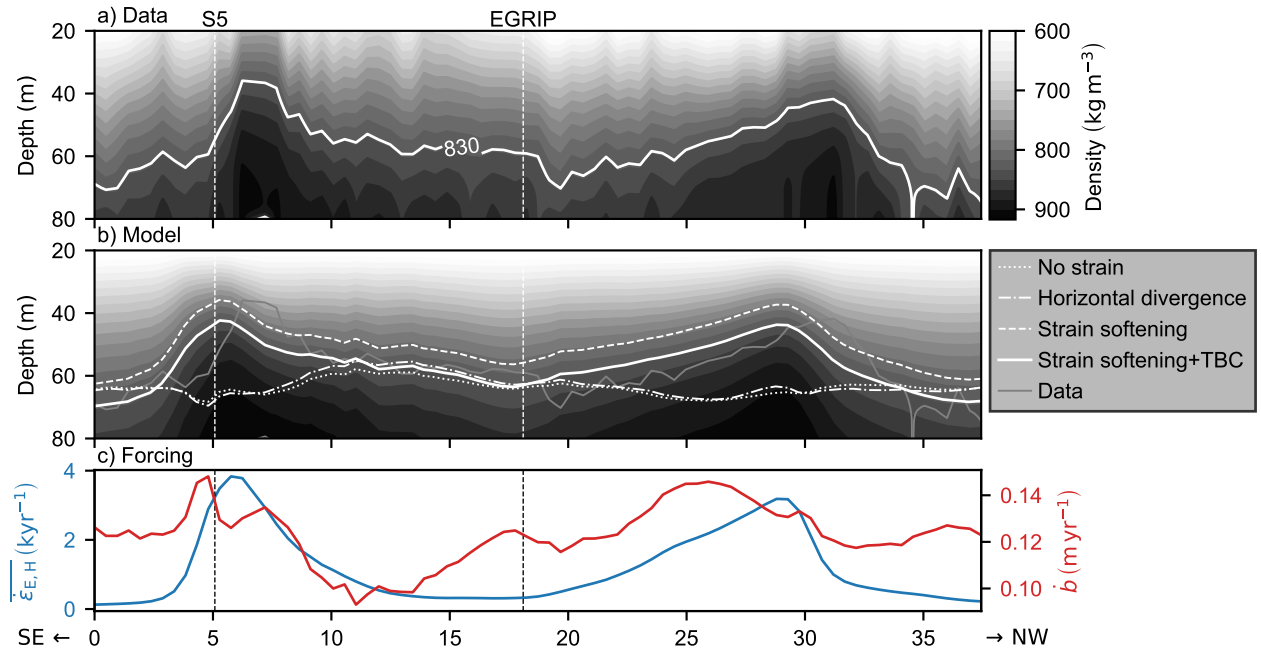


**Figure 3.** (a) Firn density profile along a cross section of NEGIS recorded by Riverman et al. (2019, Fig. 9b). The white contour line indicates the firn-ice transition. (b) Modeled firn density profile for the same location using the tuning bias corrected (TBC) strain softening model, where the white line again indicates the firn-ice transition. The latter is also shown for the cases of no strain, horizontal divergence and the uncorrected strain softening model. (c) Mean effective horizontal strain rate over the firn age and the radar-derived accumulation rate, which are used for forcing the models in (b). The dashed vertical lines indicate the locations of EGRIP and the S5 shear margin firn core site.

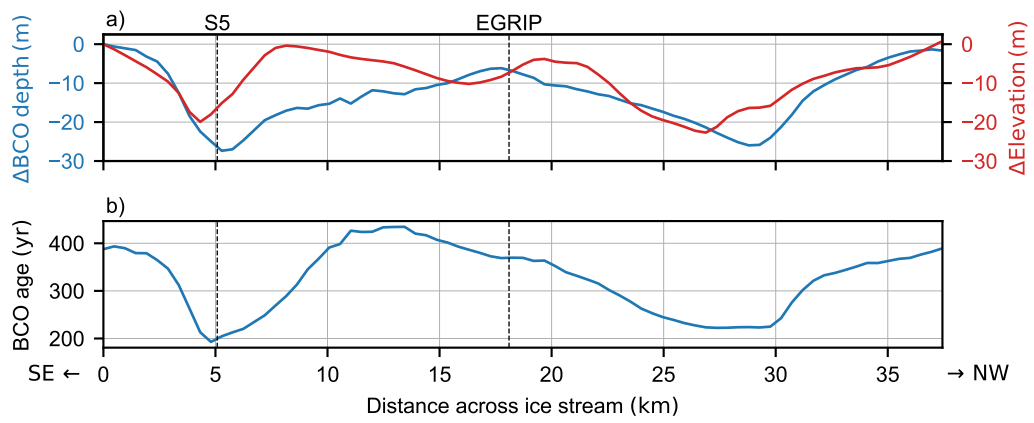


**Figure 4.** Firn properties along the NEGIS density profile, according to the tuning bias corrected strain softening model, as shown in Fig. 3b. (a) The change of the bubble-close off (BCO) depth and the surface elevation with respect to the first data point. (b) Age of the firn at bubble-close off.

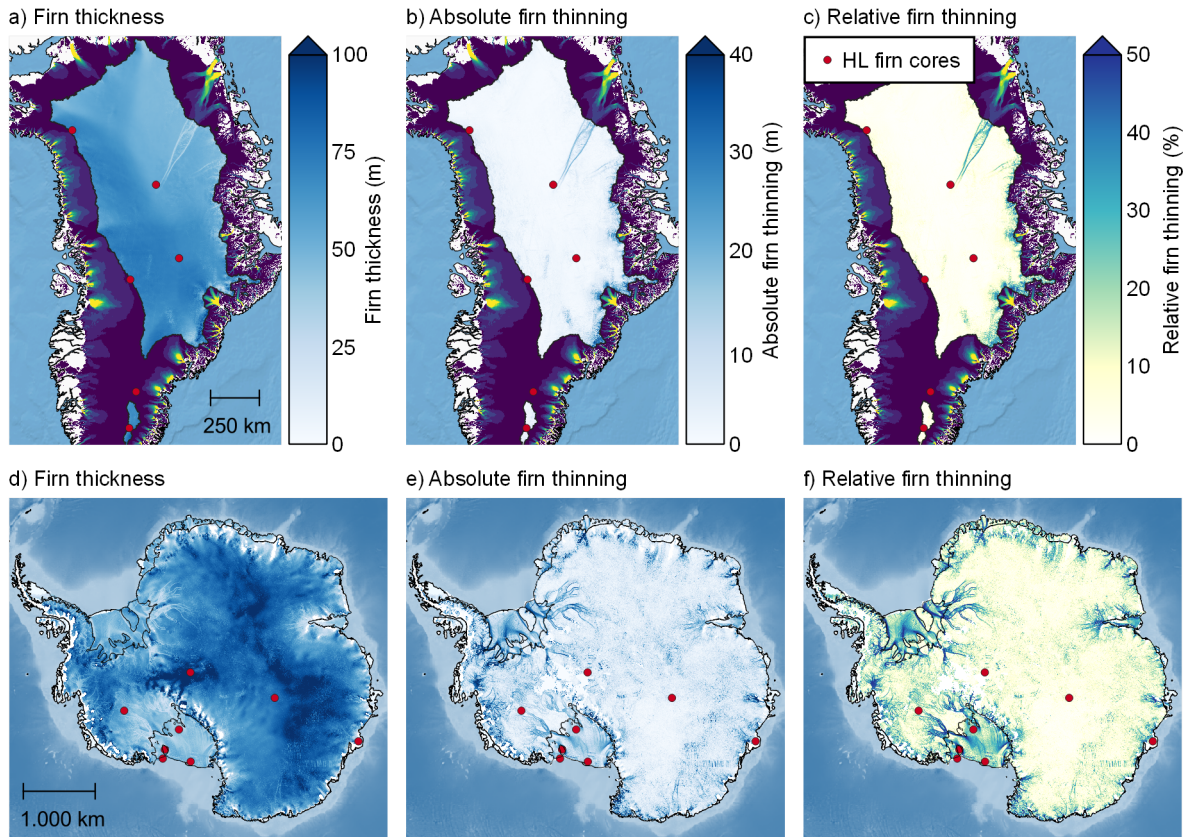


**Figure 5.** Study on the contribution of strain softening to firn densification in terms of the firn thickness over the dry zone of the Greenland ice sheet (GrIS, a-c) and the Antarctic ice sheet (AIS, d-f). (a & d) Modeled total firn thickness when strain softening is considered without the tuning bias correction. (b & e) Absolute firn thinning contribution caused by strain softening. (c & f) Relative firn thinning due to strain softening, which also illustrates by how much the densification process is accelerated by strain softening. Red dots indicate the drill locations of the firn cores that were used for tuning the empirical Herron-Langway model. Outside the dry zone of GrIS the surface velocity is shown with brighter colors indicating faster flow.